

Feature-rich plasmon excitations in sliding bilayer graphene

Chiun-Yan Lin^a, Ming-Fa Lin^{a,b,c}

^aDepartment of Physics, National Cheng Kung University, Taiwan

^bHierarchical Green-Energy Materials Research Center, National Cheng Kung University, Tainan, Taiwan

^cQuantum topology center, National Cheng Kung University, Tainan, Taiwan

November 16, 2021

Abstract

The tight-binding model is closely associated with the modified layer-based random-phase approximation to thoroughly investigate the electron-electron interactions in sliding bilayer graphene. The Coulomb interactions and intralayer and interlayer atomic interactions dominate the collective and electron-hole excitations. The unusual energy bands are directly reflected in the diverse transferred momentum-frequency phase diagrams. In general, there exist two kinds of plasmon modes during the variation of the doping level in sliding bilayer graphene, being accompanied with the complicated intraband and interband single-particle excitations. The excitation behaviors are greatly diversified by the relative shift between two graphene layers. The theoretical predictions can be verified by high-resolution experimental examinations.

In addition to the normal AA and AB stackings, the geometric structures of bilayer graphene could be manipulated by the relative shift along the specific direction, [1–8] the twisted angle between two layers, [9–11] and the modulated period due to the gradual transformation of stacking configuration [12,13] (e.g., AB/domain wall/BA/domain wallK; details in [12]). These three types of typical bilayer systems have been successfully synthesized under the various experimental methods. [14–16] Apparently, they, respectively, present the different unit cells, corresponding to the original carbon atoms in a regular hexagon, many atoms in a Morie superlattice cell, and more than one thousand atoms in a geometry-modulated periodical cell. As a result, the sliding and twisted bilayer graphenes, respectively, possess two pairs and many pairs of 2D energy bands due to the $2p_z$ orbitals, as clearly displayed along the high symmetry points in the first Brillunin zone. [7] However, the geometry-modulated bilayer graphene possesses a lot of 1D energy subbands. The first and second systems exhibit the 2D behaviors, while the third one shows the 1D phenomena. For example, the van Hove singularities belong to the dimension-dependent special structures; furthermore, the 2D and 1D parabolic bands in DOS/optical absorption spectra/imaginary parts of bare polarization functions display the shoulder and square-root asymmetric peaks, respectively. In Chap. 10, the sliding bilayer graphene is chosen for a model study, so that the asymmetry-enriched Coulomb excitations could be explored in detail.

There are certain significant studies on the diversified essential properties of the sliding bilayer graphene systems. The previous theoretical works show that the intermediate configurations between AA and AB stackings exhibit an anomalous optical phonon splitting [8] and an unusual electronic transmission. [7] By the first-principle calculations, the dependence of phonon frequency on the sliding stackings affects the polarized Raman scattering intensity, which is deduced to be available in identifying tiny misalignments in bilayer graphene. [8] Moreover, according to the combination of the generalized tight-binding model and the gradient approximation, electronic and optical properties under a uniform perpendicular magnetic field could be explored in detail. [7,17] The well-behaved,

perturbed, and undefined LLs are, respectively, associated with the normal, deviated and fully random stacking configurations (the high, middle, and low symmetries), corresponding to the Dirac-cone structures/parabolic energy bands, the distorted band structures, and the thorough destruction of Dirac points. Also the magneto-absorption spectra are characterized by a specific selection, the extra selection rules, and the absence of selection rule. However, a full comprehension of the Coulomb excitation phenomena under various stacking configurations has not been previously achieved.

The essential electronic properties, band structures and DOSs, of the sliding bilayer graphene systems are thoroughly explored by the tight-binding model, in which the position-related interlayer hopping integrals under the empirical formula are more convenient for the numerical calculations. [7] The shift-created features, the vertical/non-vertical Dirac-cone structures, the well-behaved parabolic dispersions, the highly distorted energy bands, the Fermi-momentum states, the extreme points, the saddle points, and the simple/complicated and linear/non-linear superposition of the subenvelope functions on four sublattices, will be investigated in detail. The work is focused on illustrating the close relations between the main characteristics of energy bands and wave functions and the diverse Coulomb excitation phenomena. According to two pairs of energy bands in bilayer graphenes, whether the single-particle excitation channels, the intrapair intraband, intrapair interband and interpair transitions, present an unusual dependence on the relative shift of two graphene layers and the doping level is worthy of a study. Furthermore, the form, number, frequency and intensity of special structures in the bare response functions are included under the investigations. Most important, the stacking-configuration- and doping-dependent energy loss spectra are expected to exhibit the diverse/various electron-hole boundaries, the acoustic & optical plasmon modes, the significant Landau dampings, and the critical transferred momenta. Specifically, the (momentum, frequency)-phase diagrams are evaluated for the distinct Fermi energies, where they display the screened response functions in the whole region.

The external Coulomb potential due to the incident electron beam is assumed to be

uniform on each graphene layer. The π and π^* electrons on the distinct layers will effectively screen the similar bare Coulomb potentials, leading to the charge redistributions and the induced Coulomb potentials. Moreover, the transferred momentum and frequency (q, ϕ, ω) are conserved during the dynamic electron-electron interactions, where $0^\circ \leq \phi \leq 30^\circ$ is the angle between \mathbf{q} and ΓK (the first Brilluoin zone). By the Dyson equation, the effective Coulomb potential between two electrons on the l - and l' -th layers is given by [21]

$$\epsilon_0 V_{ll'}^{eff}(\mathbf{q}, \omega) = V_{ll'}(\mathbf{q}) + \sum_{mm'} V_{lm}(\mathbf{q}) P_{mm'}^{(1)}(\mathbf{q}, \omega) V_{m'l'}^{eff}(\mathbf{q}, \omega). \quad (1)$$

The first term is the bare Coulomb potential $V_{ll}' = v_q e^{-q|l-l'|}$ (the 2D potential $v_q = 2\pi e^2/q$ associated with a 2D electron gas). The second term corresponds to the induced potential, in which the induced potential is proportional to the screening charge density using the Fourier-transform Poisson equation, and the latter is proportional to the effective potential under the linear self-consistent method. The linear coefficient, the bare polarization, which includes the layer-dependent electron-hole excitations, is expressed by

$$P_{mm'}(\mathbf{q}, \omega) = 2 \sum_k \sum_{h, h'=c, v} \sum_{n, n'} \left(\sum_s U_{smh}(\mathbf{k}) U_{sm'h'}^*(\mathbf{k} + \mathbf{q}) \right) \times \left(\sum_s U_{smh}^*(\mathbf{k}) U_{sm'h'}(\mathbf{k} + \mathbf{q}) \right) \times \frac{f(E_n^h(\mathbf{k})) - f(E_{n'}^{h'}(\mathbf{k} + \mathbf{q}))}{E_n^h(\mathbf{k}) - E_{n'}^{h'}(\mathbf{k} + \mathbf{q}) + \hbar\omega + i\Gamma}. \quad (2)$$

Specifically, the excited electron and hole in each excitation pair, which arises from the Coulomb perturbation, frequently appear on distinct layers. U_{smh} 's are the amplitudes related to the six tight-binding functions, s represents the specific A^i/B^i sublattice, and h denotes the valence/conduction state. Band-structure effects, using the layer-decomposed contributions, have been included in Eq. (2). From the detailed derivations under the Born approximation, the dimensionless energy loss function, being directly proportional to the measured EELS intensity, is defined as

$$\text{Im}[-1/\epsilon] \equiv \sum_l \text{Im} \left[-V_{ll}(\mathbf{q}, \omega) \right] / \left(\sum_{lm} V_{lm}(q)/N \right). \quad (3)$$

The denominator is the average of all the external potentials on the N -layer graphene.

Equation (3) is suitable for any emergent layered systems, such as, the group-IV and group-V 2D materials. This screened response function provides the full information on the diverse plasmon modes, and the bare one in Eq. (2) describes the single-particle (electron-hole) excitations.

The continuous stacking configurations could be achieved by a relative shift between two graphene layers. The six ones, being chosen below, clearly illustrate the diversified essential properties. One layer is gradually shifted along the armchair direction (\hat{x}) according to the following path (Fig. 1): (a) $\delta = 0$ (AA), (b) $\delta = 1/8$, (c) $\delta = 6/8$, (d) $\delta = 1$ (AB), (e) $\delta = 11/8$; (f) $\delta = 12/8$ (AA') (shift in the unit of C-C bond length). The interlayer distance is assumed to remain unchanged within the tight-binding model, while it weakly changes with the variation of stacking configuration from the VASP calculations. [20] Also, the numerical method shows that the AB stacking is most stable among all the stackings. The low-energy Hamiltonian, which mainly comes from with four $2p_z$ orbitals in a primitive unit cell, is expressed as

$$H = - \sum_{i,j} \gamma_{ij} c_i^\dagger c_j. \quad (4)$$

where γ_{ij} is intralayer or the interlayer hopping integral from the i - and j -th lattice sites. Using the well-fitting parameters in [7] the distance- and angle-dependent $2p_z$ -orbital interactions have the analytic form

$$\gamma_{ij} = \gamma_0 e^{-\frac{d-b_0}{\rho}} \left[1 - \left(\frac{\mathbf{d} \cdot \mathbf{e}_z}{d} \right)^2 \right] + \gamma_1 e^{-\frac{d-d_0}{\rho}} \left(\frac{\mathbf{d} \cdot \mathbf{e}_z}{d} \right)^2. \quad (5)$$

$\gamma_0 = -2.7$ eV is the intralayer nearest-neighbor hopping integral, $\gamma_1 = 0.48$ eV inter-layer vertical hopping integral, \mathbf{d} position vector connecting two lattice sites, $d_0 = 3.35$ Å interlayer distance, and $\rho = 0.184b$ decay length. This model is very convenient and reliable in describing the various layer-layer interactions in graphene-related sp^2 systems, such as multi-walled carbon nanotubes [18] and multilayer graphenes. [19] It has been successfully generalized to electronic properties under a uniform magnetic field, directly revealing the sliding-induced three kinds of LLs with the special optical selection rules. [7]

The low-lying band structures directly reflect the various stacking symmetries in the sliding bilayer graphene. They are equivalent about two valleys K and K', since the inversion symmetry/the equivalent A and B sublattices exists in all the systems. The AA bilayer stacking, as shown in Fig. 2(a), the first and the second pairs of Dirac cones centered at the K/K' point have the initial energies $E^{c,v} = 0.32$ eV and -0.36 eV, respectively. A strong overlap of two vertical Dirac cones indicates the existence of free electrons and holes. When a relative shift gradually grows, e.g., $\delta = 1/8$ in Fig. 2(b), a strong hybridization appears between the conduction states of the lower cone and the valence states of the upper cone. This leads to distorted Dirac-cone structures along \hat{k}_x with a created arc-shaped stateless region near E_F , indicating the reduce of the free electron/hole density and holes. Apparently, the conduction and valence bands only touch each other at two points on the edge of the arc-shaped region; furthermore, these points belong to the Fermi-momentum states (k_{FS}) within the sliding of AA \rightarrow AB. Moreover, there are two pairs of saddle points on the top and bottom of the arc-shaped stateless region within the range $0 < \delta < 5/8$, where the critical displacement is $\delta_c \sim 5/8$. The conservation of the number of electronic states means that the low-energy states near the K point are transferred to its neighbor regions, especially at the induced saddle points. However, the energies of two pairs of saddle points are nearly the same for small shifts (energy difference of less than 0.02 eV). With the further increase of shift, the arc-shaped region expands quickly, and energy dispersions are highly distorted at $\delta = 6/8$ (Figure 3c), where the saddle-point energies are completely split. The complete separations of the upper and the lower Dirac cones clearly illustrate that two pairs of energy bands are reformed at the the different initial energies. The band-edge states, corresponding to the first and the second pairs of energy bands, have $E^{c,v} \sim 0$ and $E^c = 0.32$ eV & $E^v = -0.36$ eV, respectively.

Also, a further change from $\delta = 1$ to $12/8$ leads to dramatic transformations of low-lying band structures. As is clear from Fig. 2(d), the AB stacking possesses two pairs of parabolic dispersions, being characterized by a weak band overlap near E_F . With increments of relative shifts, the parabolic bands of the first pair are strongly distorted along \hat{k}_y and

$-\hat{k}_y$ simultaneously, as apparently shown at $\delta = 11/8$ in Fig. 2(e). The region outside the created eye-shape region, with two new Dirac points at distinct energies, grows rapidly. Furthermore, two neighboring conduction (valence) bands form strong hybrids. Finally, two pairs of isotropic Dirac cones are formed in the AA' stacking ($\delta = 12/8$ in Fig. 2(f)), where the linearly intersecting Dirac points are situated at different wave vectors with $E^{c,v} = -0.11$ eV and 0.1 eV. The tilted cone axes lie in the opposite directions for the conduction and valence bands, being clearly identified from the distinct loops with a constant energy measured from the current Dirac point. [7]

The diverse electronic structures are revealed as the various vHSs DOSs, as clearly shown in Fig. 3. The low-energy DOSs exhibit two types of vHSs near the Fermi level, namely, plateau and dip structures. The former is due to the linear energy dispersions across E_F , corresponding to the AA stacking and the configurations close to the AA stacking (Figs. 2(a), 2(e) and 2(f)). However, the latter comes from the band-edge states of parabolic energy bands (Figs. 2(b)-2(d)). Such DOSs are proportional to the free carrier densities created by the interlayer atomic interactions, so that they dominate the low-frequency plasmons in the sliding bilayer graphene systems. Except for the well-behaved AA, AB, and AA stackings, the other stackings display symmetric peak structures at lower energies ($\sim \pm 0.2$) eV), being induced by the new saddle points at the top and bottom of the arc-shaped stateless region (Figs. 2(b), 2(c) and 2(e)). The number and energy of significant peaks are sensitive to the relative shift (details in Ref. [20]).

The unusual band structures of the sliding bilayer systems will create the diverse Coulomb excitation phenomena. These systems possess four atoms in a primitive unit cell under the theoretical calculations, so that the single-particle layer-dependent polarization functions have four components or two independent elements ($P_{11}=P_{22}$ & $P_{12} = P_{21}$). The special structures in P_{11} and P_{12} directly originate from the Fermi momentum states and the band-edge states/the critical points in the energy-wave-vector space, in which their forms could be examined/identified from the energy dispersions, dimensionalities, and Kramers-Kronig relations. They are very useful in determining the distinct/composite

electron-hole excitation regions and the Landau dampings of the plasmon modes.

The pristine bilayer AA stacking exhibits the rich special structures in the bare polarization functions, as clearly shown on Figs. 4(b) and 4(a) by the black curves. The first square-root asymmetric peaks in $Im[P_{11}]$ and $Im[P_{12}]$ (the black curves), corresponding to the form of $1/\sqrt{\omega_- - \omega}$, is located at $\omega_- \sim 3.0\gamma_0 bq$. By the kramers-kronig relations, the real parts are square-root divergent in the opposite form. Such prominent structures are due to the intra-pair intraband transitions, namely $1v \rightarrow 1v$ and $2c \rightarrow 2c$. Furthermore, they originate from the Fermi-moment states in the linear dispersions. [21] Such excitations could only survive at small transferred momenta ($< 0.1 \text{ \AA}^{-1}$) comparable to the Fermi momenta. And then, the intra-pair electronic excitations are forbidden within a sufficient wide frequency range of $\omega_- < \omega < \omega_+$ ($\sim 0.1 - 0.8 \text{ eV}$). They are obviously indicated by the vanishing the single-particle electronic polarizations ($Im[P_{11}] = Im[P_{12}] = 0$). The absence of the intra-pair interband transitions will create the significant 2D plasmon modes due to the free electrons and holes (Fig. 7). Such excitations, $1v \rightarrow 1c$ & $2v \rightarrow 2c$, will come to exist only for the enough high transferred frequency of $\omega > \omega_+$, e.g., four $1/\sqrt{\omega - \omega_+}$ -form asymmetric peaks at $\omega > 0.8 \text{ eV}$. It should be noticed that the specific intra-pair interband excitation channels might induce two close peaks as a result of the asymmetric Dirac cones/the distinct linear energy dispersions about the K/K' point. However, only one peak is revealed in the previous investigation on the same system. The minor differences lie in the theoretical model, since the current interlayer interactions include more non-vertical hopping integrals.

The small shift deviated from the AA stacking might induce the similar excitation behaviors and the significant differences simultaneously. The $\delta = 1/8$ bilayer system also displays one-/four-peak structure associated with the intrapair intraband/interband excitations in the single-particle polarization functions, as clearly illustrated by the black curves in Figs. 4(e)-4(h) under small transferred momenta. Specifically, the intensity of the lowest-frequency asymmetric peak obviously presents a great decrease, directly reflecting the reduced screening ability. The decline of free carrier density (the decrease of DOS

at the Fermi level) and the creation of the stateless eye-shape region are responsible for the weakened Coulomb response. Moreover, the higher-frequency electronic excitations, which arise from the intrapair interband transitions, are available in a more wide ω -range, mainly owing to the enhanced asymmetry of energy spectrum. It should be noticed that the saddle points in the low-lying energy bands, with a very high DOS, do not present any special structures in bare polarization functions. However, the valence and conduction could induce a prominent peak structure in the optical absorption spectrum. [17] Apparently, this important difference between the Coulomb and EM-wave excitations mainly lie in the non-vertical and vertical transitions, respectively.

There exists the dramatic transformation in low-energy electronic properties under a sufficiently large shift, and so do the Coulomb excitation phenomena. The $\delta = 6/8$ bilayer graphene, as clearly shown in Figs. 5(a)-5(d) by the black solid curves, exhibits the single-particle excitations in the overall region. This result obviously indicates more available excitation channels due to the abnormal superposition of the four subenvelope functions on the first and second layers. The intra- and inter-pair interband transitions, $1v \rightarrow 1c$, $1v \rightarrow 2c$, $2v \rightarrow 1c$ & $2v \rightarrow 2c$, are very efficient during the non-vertical Coulomb excitations. Moreover, three kinds of special structures appear the imaginary and real parts of polarization functions, namely, the square-root asymmetric peaks, the logarithmically symmetric peaks, and the shoulders, in which the latter two structures are consistent with each other in the principle-value integrations. Such structures, respectively, originate from the Fermi-momentum states with the linear energy dispersions, the saddle points, and the band-edge states of the parabolic bands. The latter two structures are consistent with each other in the principle-value integrations. For example, under a specific $q = 0.005$ $1/\text{\AA}$, the strong threshold response appears at ~ 0.022 , being due to the Fermi-momentum initial/final states in the first pair of valence and conduction bands. The second symmetric/shoulder structure at ~ 0.24 eV presents the logarithmic/discontinuous form in the imaginary/real parts of polarization functions [Figs. 5(b) & 5(d)/Figs. 5(a) & 5(c)]. This structure is closely related to the occupied and unoccupied saddle points in the first pair of

interband transitions. With the increasing frequency, the interpair interband excitations, $1v \rightarrow 2c$ & $2v \rightarrow 1c$, come to exist within the range of $0.45 \text{ eV} < \omega < 0.62 \text{ eV}$, clearly revealing three special structures. It is very difficult to identify their specific forms, since energy bands display the strong asymmetry about the Fermi level (Fig. 2(c)). Finally, the band-edge states of the second parabolic valence/conduction bands could create an obvious shoulder/logarithmic peak at $\sim 0.88 \text{ eV}$ in the imaginary-/real-part bare response functions. The active single-particle excitations will become the very high barrier in generating the undamped plasmon modes.

The polarization functions become more concise under the normal AB stacking of $\delta = 1$, compared with those of the other stackings. They are clearly illustrated by the solid black curves in Figs. 5(e)-5(h). The well-behaved symmetric and anti-symmetric superposition of four subenvelope functions has lead to the absence of the interpair interband excitations. Furthermore, by using the intrapair interband excitations, the well-known parabolic dispersions near the band-edge states only induce the shoulder/logarithmic peak structures in the $Im[P_{11}]$ & $Im[P_{12}]/Re[P_{11}]$ & $Re[P_{12}]$ [Figs. 5(f) & 5(h)/ Figs. 5(e) & 5(g)]. The special structures at $\omega \sim 0.01$ & 0.91 eV 's. respectively, originate from $1v \rightarrow 1c$ & $2v \rightarrow 2c$. Specifically, the imaginary parts of bare response functions could survive in most of (momentum, frequency)-phase diagram. The 2D plasmon modes are expected to experience the rather strong Landau dampings; that is, they might be difficult to present the prominent peak structures in the energy loss spectra.

The further large deviation from the AB stacking, for example, $\delta = 11/8$ (the black solid curves in Figs. 6(a)-6(d)), also creates the complicated and unique Coulomb excitations, as revealed in $\delta = 6/8$ (Figs. 5(a)-5(d)). According to the range of frequency, the diverse single-particle Coulomb excitations cover the intrapair interband transitions [$1v \rightarrow 1v$ & $2c \rightarrow 2c$], the interpair interband channels [$2v \rightarrow 1c$ & $2c \rightarrow 1c$], and the intrapair interband scatterings [$1v \rightarrow 1c$ & $2v \rightarrow 2c$]. Their special structures, which directly reflect the unusual band structure (Fig.2(e)), respectively, come to exist at $\omega \sim 0.03 \text{ eV}$, $0.30 - 0.32 \text{ eV}$, and $0.74 - 0.84 \text{ eV}$. The low-lying, distorted, and non-vertical Dirac

cones, which are accompanied with the higher-/deeper-energy parabolic conduction/valence band in the first/second one, are responsible for the threshold/first square-root asymmetric peak. Furthermore, this rather asymmetric energy spectrum about $E_F = 0$ induces the second structures arising from $2v \rightarrow 1c$ & $2c \rightarrow 1c$, but not due to $1v \rightarrow 2c$ & $1c \rightarrow 2c$. It should be noticed that the excitation channels of the latter cannot generate any special structures under the absence of the Fermi-momentum and parabolic band-edge states. Finally, the intrapair interband transitions dominate the higher-frequency polarization functions and present two neighboring special structures (red or black circles) for the specific $1v \rightarrow 1c/2v \rightarrow 2c$. The splitting excitation phenomena purely come from the highly hybridized energy bands, since the conduction/valence band of the first/second pair possesses the separated Dirac-cone and parabolic dispersions.

After the final transformation of $\delta = 11/8 \rightarrow 12/8$, the composite energy dispersions become the non-vertical two Dirac-cone structures, leading to the disappearance of certain excitation channels/phenomena. The bare response functions of the AA' stacking, being clearly illustrated in Figs. 6(e)-6(h), exhibit the unusual square-root asymmetric peaks at $\omega \sim 0.03$ eV, 0.36 eV; 0.78 & 0.86 eVs. They arise from the Fermi-momentum states in the linear energy dispersions, as discussed earlier in the AA stacking. Such structures, respectively, correspond to $[1v \rightarrow 1v \text{ \& } 2c \rightarrow 2c]$, the interpair interband channels $[2v \rightarrow 1c]$, and the intrapair interband scatterings $[1v \rightarrow 1c \text{ \& } 2v \rightarrow 2c]$. The interpair interband channel of $2c \rightarrow 1c$ is forbidden as a result of the well-behaved functions in the linear superposition of four subenvelope functions. Moreover, there are no excitation splittings in the higher-frequency channels, since the parabolic conduction/valence band disappears in the first/second Dirac cone.

The dopings effects create a great diversity in the single- and many-particle electronic excitations. The sliding bilayer graphene is assumed to keep the rigid band structure after the electron/hole doping. The blue shift of E_F is chosen for a model study. From the viewpoints of Coulomb excitations, the energy spectra about the Fermi level become more asymmetric. This might lead to the dramatic changes in the bare response func-

tions. According to three categories of excitation frequency ranges, the drastic/negligible variations of the special structures are described as follows. As for the AA stacking, the square-root asymmetric peak at $\omega \sim 3\gamma_0 bq$ almost remains the same in the presence of any dopings, e.g., the approximately identical P_{11} and P_{12} under $E_F = 0.4$, 0.2 and 0 eVs (the blue, red; black curves in Figs. 4(a)-4(d)). Such result directly reflects the fact that the two Dirac-cone structures are highly overlapping and straightly vertical (Fig. 2(a)). However, the strength of polarization functions in the $\delta = 1/8$ stacking is enhanced by the increase of E_F , as shown in Figs. 4(e)-4(h). It is sensitive to the number of the Fermi-momentum states (Fig. 2(b)). With the further increase of shift, the $\delta 6/8$ stacking presents the unusual response functions in Figs. 5(a)-5(d). The two kinds of excitation channels, both intrapair intraband and interband transitions [$1c \rightarrow 1c$ & $1v \rightarrow 1c$], replace the original intrapair interband transition associated with the Fermi-momentum and saddle-point states (Fig. 2(c)). The enlarged square-root peak (the first structure) is attributed to more Fermi-momentum states. Furthermore, the logarithmically symmetric peak in the imaginary part of polarization function (the second structure) is roughly substituted by the shoulder structure. Specially, the AB stacking (Figs. 5(e)-5(f)), with two pairs of parabolic bands (Fig. 2(d)), exhibits the dramatic transformation, the variation from the shoulder/symmetric peak structure into the square-root asymmetric peak for $Im[P_{11}]$ & $Im[P_{12}]/Re[P_{11}]$ & $Re[P_{12}]$, where the original mechanism of $1v \rightarrow 1c$ is replaced by $1c \rightarrow 1c$. It should be noticed that the former channel is transferred to the next frequency range. Finally, Figs. 7(a)-7(h) show that the identical doping effects are revealed in the $\delta = 11/8$ & $12/8$ bilayer graphene systems, being related to the similar non-vertical Dirac-cone structures (Fig. 2(e)-2(f)). That is to say, the square-root asymmetric peak is strengthened by the increment of free carrier density.

Concerning the second category of special structures, the $\delta = 0$ and $\delta = 1/8$ stackings remain featureless in the range of $0.2 \text{ eV} < \omega < 0.6 \text{ eV}$ under any dopings/different E_F s, as clearly shown in Figs. 4(a)-4(h). The unchanged wave functions under the rigid-band approximation are responsible for the vanishing interpair interband excitations. Such tran-

sitions in the $\delta = 6/8$ stacking appear at the higher-frequency range of $0.4 \text{ eV} < \omega < 0.6 \text{ eV}$. Three kinds of channels, $[1v \rightarrow 2c, 2v \rightarrow 1c]$ & $1c \rightarrow 2c$, present more special structures in which the third one is purely induced by the doping effect. Specially, the AB stacking can display the strong responses within the range of $0.36 \text{ eV} < \omega < 0.48 \text{ eV}$, strongly depend on the free carrier densities. The new channels are associated with the intrapair interband and the interpair excitations, namely, $[1v \rightarrow 1c, \& 1c \rightarrow 2c]$. They only survive at a finite E_F ; furthermore, the latter is not suppressed by the well-behaved wave functions, being thoroughly different from the vanishing $1v \rightarrow 2c$ & $2v \rightarrow 1c$. The interpair transitions of $2c \rightarrow 1c$ & $2v \rightarrow 1c$, corresponding to $0.10 \text{ eV} < \omega < 0.36 \text{ eV}$, keep the same for the $\delta = 11/8$ stacking. However, there are more special structures and wider distributions, further illustrating the close relations between energy spectrum and E_F . Also, these two channels occur in the AA' system, while the former one is dominated by the carrier dopings. For any sliding bilayer systems in Figs. 4-6, the critical excitation channels at $0.75 \text{ eV} < \omega < 0.95 \text{ eV}$ (the third category) are not affected by a finite E_F , mainly owing to the higher/deeper-energy bands with the specific energy dispersions. Apparently, the intensity, number, form, and frequency of the special structures are very sensitive to the change of the free carrier densities. In addition, the main features of the bare response functions also depend on the magnitude of transferred momenta, e.g., those under $q = 0.02 \text{ 1/\AA}$ and $E_F = 0.2 \text{ eV}$ (the green curves in Figs. 4-6).

The energy loss spectra of the sliding bilayer systems could provide the diverse screened phenomena, in which the 2D plasmon modes might be damped by the various electron-hole pair excitations. As to the pristine AA stacking, Fig. 7(a) clearly illustrates that there are two significant peaks at $\omega_P \sim 0.22 \text{ eV}$ and 1.095 eV under $q = 0.005 \text{ 1/\AA}$, especially for the very prominent former. The first plasmon mode, which is due to the intrapair intraband excitations (Fig. 4(a)-4(d)), has the excitation frequency much higher than the single-particle one (0.055 eV). This plasmon is the collective charge oscillations of free electrons and holes purely induced by the rather strong interlayer hopping integrals, The collective excitations do not experience any Landau dampings, since both intrapair interband and

interpair transitions are absent at small transferred momenta. Another higher-frequency plasmon mode arises from the intrapair interband channels; furthermore, their strength is weakened by the single-particle excitations (inset in Fig. 8(a)). However, the intensities of plasmon peaks are obviously reduced in the $\delta = 1/8$ stacking, as indicated in Fig. 7(b). This result directly reflects the low-lying distorted Dirac-cone structures (Fig. 2(b)) with the lower free carrier density and the stronger Landau dampings. As to the plasmon frequencies, only a small enhancement/decrease is revealed in the first/second mode. With the further increasing shift, such plasmon modes present the dramatic changes in their intensities. They might be very weak in the $\delta = 6/8$ and $\delta = 1$ stackings (Figs. 7(c) and 7(d)), or they would be rather difficult to be observed in the energy loss spectra. The main reason is too low DOS at E_F /free carrier density. Finally, the second plasmon peak almost disappears for the $\delta = 11/8$ and $\delta = 12/8$ systems (Figs. 7(e) and 7(f)). The intensity of the first plasmon mode is much lower/higher than of AA/AB. Such results should be attributed to the non-vertical Dirac-cone band structures (Fig. 2(2) and 2(f)).

The electron or hole doping can create the rich and unique phenomena in the plasmon peaks of the energy loss spectra, mainly owing to the enhanced asymmetry of energy spectra. For the AA stacking (Fig. 8(a)), the frequency and strength of two plasmon modes do not present a simple and monotonous relation in the increase of the Fermi energy, especially for those of the former. For example, the first plasmon mode at $E_F = 0.4$ eV (the blue curve) only presents a weaken peak. The main mechanism is that the Fermi level, being above and close to the Dirac point (Fig. 2(a)), has lead to the non-uniform distributions of free electrons and holes. The similar results are revealed in the $\delta = 1/8$ stacking, as indicated in Fig. 8(b). However, the first/second plasmon of the $\delta = 6/8$ stacking is largely/somewhat strengthened; furthermore, it comes to exist for the AB stacking. In these two systems, the increase of free conduction electrons is responsible for the enhanced/emergent plasmon mode. At last, the doping effect on the $\delta = 11/8$ and $\delta = 12/8$ stackings is to increase the intensity and frequency of the first plasmon, while it cannot generate the second plasmon mode. Such effect is much stronger than that in the AA

stacking (Fig. 7(a)), being related to the smaller Dirac-point energies (Fig. 2(b)).

The sliding bilayer systems obviously exhibit the geometry- and doping-diversified Coulomb excitation phenomena by illustrating the rich (momentum, frequency)-phase diagrams, as indicated in Figs. 8-10. For the pristine graphenes, Fig. 8 clearly displays the shift-induced dramatic variations in electronic excitations, where two plasmon modes and the electron-hole excitation boundaries are very sensitive to the stacking configurations/the low-lying energy bands. The regions of single-particle excitations, as indicated by the dashed and solid lines, are mainly determined by the Fermi momenta and band-edge states. Two kinds of collective excitations, corresponding to the red/yellow/green curves, could only survive in the $\delta = 0$ and $\delta = 1/8$ systems (Figs. 8(a) and 8(b)). From the momentum dispersion relation, the first and second plasmons, respectively, belong to the acoustic and optical modes. The frequency of the former has the \sqrt{q} relation at small momenta, being similar to that of 2D electron gas. That is to say, free electrons and holes, respectively, in two distinct Dirac cones simultaneously contribute to the collective charge oscillations at long wavelength. This plasmon is completely undamped within $q < 0.05 \text{ \AA}^{-1}$ and experiences the rather strong intrapair interband dampings after a critical momentum of $q_c > 0.1 \text{ 1/\AA}$. Apparently, it is relatively difficult to observe the latter from the weaker energy loss spectra. The very similar results in these two systems suggest that a small shift of two graphene layers does not drastically alter the main features of electronic excitations. As a result, two plasmon modes almost disappear for the $\delta = 6/8$ and $\delta = 1$ stackings (figs. 8(c) and 8(d)) except that the acoustic plasmon exists in the former at very small qs . This result reflects the fact that the free carrier density due to the interlayer atomic interactions is very low. Concerning the $\delta = 11/8$ and $\delta = 12/8$ bilayer graphenes (Figs. 8(e) and 8(f)), only the first plasmon modes, with the lower intensity, is revealed at $q_c \sim 0.05 \text{ 1/\AA}$. Apparently, the AA' stacking is quite different from the AA system in the regions of electron-hole excitations and the existence of plasmon modes. The great differences are attributed to the tilted/non-tilted axis of the two distinct Dirac-cone structures and the energy spacing between the Dirac points/the free carrier density.

Apparently, the blue shift of the Fermi level results in the dramatic changes and the different effects on the Coulomb excitation spectra, as clearly shown in Figs. 9(a)-9(f) and 10(a)-10(f). Of course, the electron-hole boundaries largely vary with the increase of E_F (the dashed and solid curves). As to the AA and $\delta = 1/8$ bilayer stackings, the same carrier density of free electrons and holes becomes non-homogenous during the increment of E_F (Figs. 2(a) and 2(b)), in which the former and the latter, respectively, grows and declines (even disappears at $E_F = 0.4$). This hinders the efficiency of the collective charge oscillations and thus reduces the plasmon strength in the screened response spectrum. The acoustic plasmon mode directly presents the decrease of the undamped momentum range and the critical transferred momentum, e.g., the most significant loss spectra in Figs. 8(a)-8(b), Figs. 9(a)-9(b) and 10(a)-10(b), respectively, under $E_F = 0, 0.2$ eV and 0.4 eV. On the other hand, the adjustment of E_F has greatly enhanced the carrier density of free conduction electrons in the $\delta = 6/8$ and AB systems (Figs. 2(c) and 2(d)). The first plasmon mode comes to exist at any doping levels (Figs. 9(c)-9(d) and Fig. 10(c) and 10(d)), while the second one appears only at the sufficiently high Fermi level (e.g., $E_F = 0.4$ eV in Figs. 10(c) & 10(d)). A simple relation between the acoustic plasmon strength and the Fermi energy is absent for these two kinds of stackings. The E_F -enhanced asymmetric effects on the energy bands of the $\delta = 11/8$ and $\delta = 12/8$ bilayer stackings (Figs. 2(e) and 2(f)) are to largely strengthen the collective oscillation frequency of the acoustic plasmon, but it cannot create the higher-frequency optical one. Also noticed ω_P of the first mode grows with the increasing Fermi level, and its strength does not present a concise E_F -dependence.

Obviously, for the sliding pristine bilayer systems, the Coulomb and electromagnetic wave perturbations present rather different bare response functions, mainly due to the non-vertical and vertical scatterings. The electronic excitations frequently appear at a finite transferred momentum, while the optical absorption spectra correspond to the $q \rightarrow 0$ transitions. The intrapair intraband excitations are forbidden in the latter, so that the optical gaps come to exist in the semi-metallic AA and AA' stackings with the higher

free carrier density. There are no square-root asymmetric peaks in the optical spectral functions even at the higher frequency. Only simple shoulders and few logarithmically symmetric peaks are revealed as the optical absorption structures. That is to say, the splitting special structures are absent under the vertical transitions. In short, the Coulomb excitations could provide more information about the shift-enriched energy bands and wave functions, compared with the optical absorptions.

Acknowledgments This work was supported in part by the National Science Council of Taiwan, the Republic of China, under Grant Nos. NSC 105-2112-M-006 -002 -MY3 and National Research Foundation of Korea (201500000002559).

References

- [1] A. Daboussi, L. Mandhour, J. N. Fuchs and S. Jaziri, Phys. Rev. B **89**, 085426 (2014).
- [2] A. M. Popov, I. V. Lebedeva, A. A. Knizhnik, Y. E. Lozovik and B. V. Potapkin, Phys. Rev. B **84**, 045404 (2011).
- [3] J. Zheng, P. Guo, Z. Ren, Z. Jiang, J. Bai and Z. Zhang, Appl. Phys. Lett. **101**, 083101 (2012).
- [4] Y. W. Son, S. M. Choi, Y. P. Hong, S. Woo and S. H. Jhi, Phys. Rev. B **84**, 155410 (2011).
- [5] K. W. Lee and C. E. Lee, Sci. Rep. **5**, 17490 (2015).
- [6] S. Bhattacharyya and A. K. Singh, Carbon **99**, 432 (2016).
- [7] Y. K. Huang, S. C. Chen, Y. H. Ho, C. Y. Lin and M. F. Lin, Sci. Rep. **4**, 7509 (2014).
- [8] S. M. Choi, S. H. Jhi and Y. W. Son, ACS Nano, **7**, 7151 (2013).
- [9] V. Perebeinos, J. Tersoff and P. Avouris, Phys. Rev. Lett. **109**, 236604 (2012).
- [10] A. I. Cocemasov, D. L. Nika and A. A. Balandin, Phys. Rev. B **88**, 035428 (2013).
- [11] J. M. B. Lopes dos Santos, N. M. R. Peres and A. H. Castro Neto, Phys. Rev. Lett. **99**, 256802 (2007).
- [12] B. L. Huang, C. P. Chuu and M. F. Lin, arXiv:1805.10775v2.
- [13] I. Martin, Y. M. Blanter and A. F. Morpurgo, Phys. Rev. Lett. **100**, 036804 (2008).
- [14] L. Jiang, S. Wang, Z. Shi, C. Jin, M. I. B. Utama, S. Zhao, Y. R. Shen, H. J. Gao, G. Zhang and F. Wang, Nat. Nanotech. **13**, 204 (2018).
- [15] X. Feng, S. Kwon, J. Y. Park and M. Salmeron, ACS Nano **7**, 1718 (2013).

- [16] Z. Liu, J. R. Yang, F. Grey, J. Z. Liu, Y. L. Liu, Y. B. Wang, et al., Phys. Rev. Lett. **108**, 205503 (2012).
- [17] C. Y. Lin, T. N. Do, Y. K. Huang and M. F. Lin, IOP Concise Physics. San Raefel, CA, USA: Morgan & Claypool Publishers, 2017.
M. Koshino, Phys. Rev. B **88**, 115409 (2013).
- [18] F. L. Shyu and M. F. Lin, J. Phys. Soc. Jpn. **68**, 3806 (Letter; 1999).
- [19] C. Y. Lin, J. Y. Wu, Y. J. Ou, Y. H. Chiu and M. F. Lin, Phys. Chem. Chem. Phys. **17**, 26008 (2015).
- [20] N. T. T. Thuy, S. Y. Lin, O. Glukhova and M. F. Lin, J. Phys. Chem. C. **119**, 10623 (2015).
- [21] J. H. Ho, C. L. Lu, C. C. Hwang, C. P. Chang, and M. F. Lin, Phys. Rev. B **74**, 085406 (2006).

Figure Captions

Figure 1: Geometric structures of bilayer graphene a shift relative along the armchair direction: (a) $\delta = 0$ (AA), (b) $\delta = 1/8$, (c) $\delta = 6/8$, (d) $\delta = 1$ (AB), (e) $\delta = 11/8$; (f) $\delta = 12/8$ (AA').

Figure 2: The 3D low-lying energy bands of the sliding bilayer graphene systems under (a) $\delta = 0$, (b) $\delta = 1/8$, (c) $\delta = 6/8$ (d) $\delta = 1$ (e) $\delta = 11/8$ and (f) $\delta = 12/8$.

Figure 3: The low-energy densities of states under the various shifts: (a) $\delta = 0$, (b) $\delta = 1/8$, (c) $\delta = 6/8$, (d) $\delta = 1$, (e) $\delta = 11/8$, and (f) $\delta = 12/8$ (AA').

Figure 4: The two independent bare polarization functions under $[q=0.005 \text{ 1/\AA}, \phi = 0^\circ; E_F = 0, 2 \& 0.4 \text{ eVs}]$ and $[q=0.02 \text{ 1/\AA}; E_F = 0, 2 \text{ eV}]$ for the $\delta = 0$ bilayer stacking: (a) $Re[P_{11}]$, (b) $Im[P_{11}]$, (c) $Re[P_{12}]$, and $Im[P_{11}]$. Similar plots of the $\delta = 1/8$ system in (e)-(h).

Figure 5: Similar bare response functions in Fig. 4, but displayed for the $\delta = 6/8$ and $\delta = 1$ bilayer graphenes in (a)-(d) and (e)-(h), respectively.

Figure 6: Similar single-particle excitation functions in Fig. 4, but illustrated by the $\delta = 11/8$ and $\delta = 12$ bilayer graphene systems, respectively, in (a)-(d) and (e)-(h).

Figure 7: The energy loss spectra under $[q=0.005 \text{ 1/\AA}, \phi = 0^\circ, E_F = 0, 0.2 \& 0.4 \text{ eVs}]$ and $[q=0.02 \text{ 1/\AA}; E_F = 0, 2 \text{ eV}]$ for the sliding bilayer systems: (a) $\delta = 0$, (b) $\delta = 1/8$, (c) $\delta = 6/8$, (d) $\delta = 1$, (e) $\delta = 11/8$, and (f) $\delta = 12/8$. Also shown in the insets are the enlarged higher-frequency results.

Figure 8: The (momentum, frequency)-phase diagrams of the pristine sliding bilayer graphenes: (a) $\delta = 0$, (b) $\delta = 1/8$, (c) $\delta = 6/8$, (d) $\delta = 1$, (e) $\delta = 11/8$, and (f) $\delta = 12/8$.

Figure 9: Similar plots as Figs. 8(a)-8(f), but shown for $E_F = 0.2$.

Figure 10: Similar plots as Figs. 9(a)-9(f), indicating the distinct doping effects at $E_F = 0.4$.

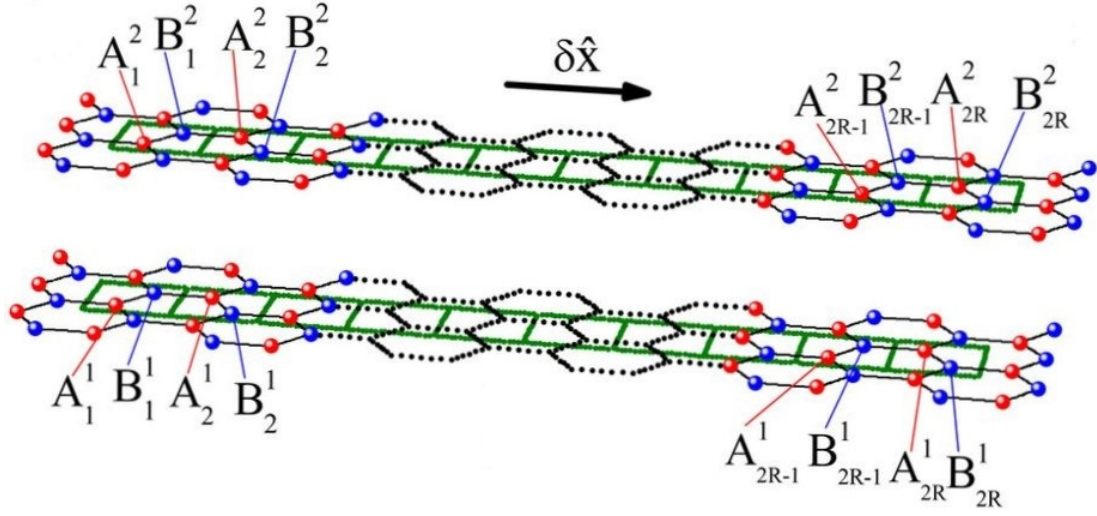


Figure 1: Geometric structures of bilayer graphene a shift relative along the armchair direction: (a) $\delta = 0$ (AA), (b) $\delta = 1/8$, (c) $\delta = 6/8$, (d) $\delta = 1$ (AB), (e) $\delta = 11/8$; (f) $\delta = 12/8$ (AA').

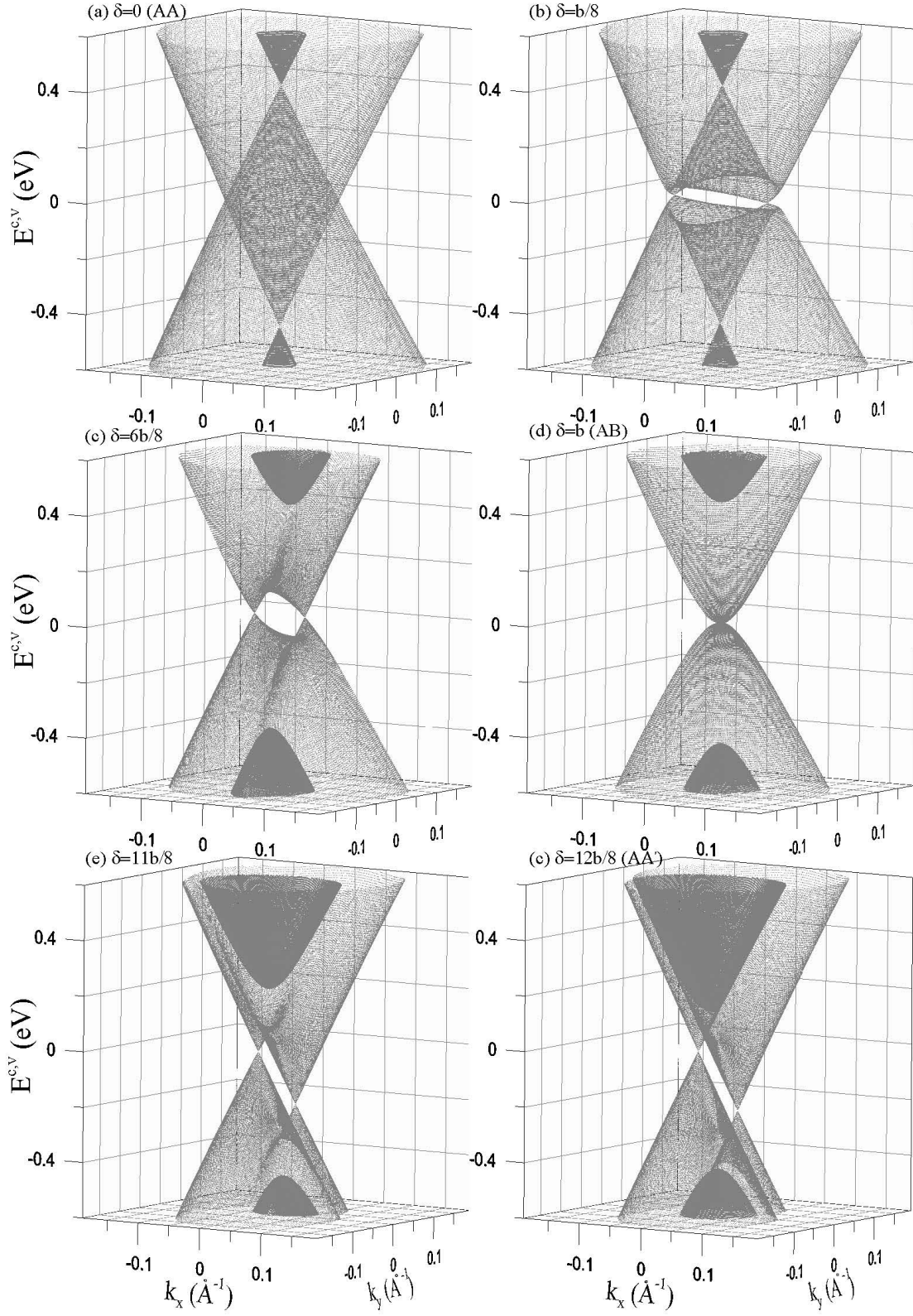


Figure 2: The 3D low-lying energy bands of the sliding bilayer graphene systems under (a) $\delta = 0$, (b) $\delta = 1/8$, (c) $\delta = 6/8$ (d) $\delta = 1$ (e) $\delta = 11/8$ and (f) $\delta = 12/8$.

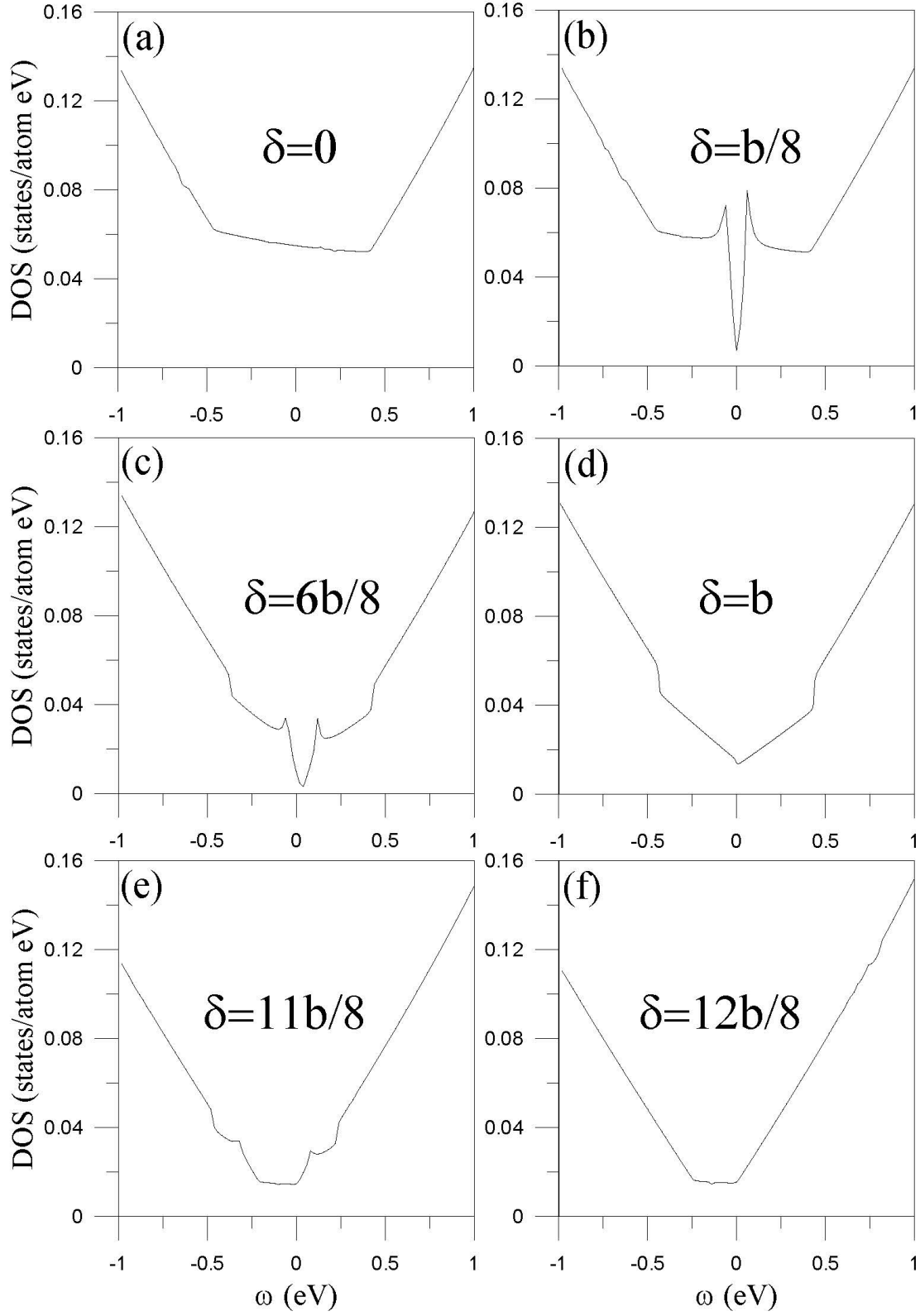


Figure 3: The low-energy densities of states under the various shifts: (a) $\delta=0$, (b) $\delta=1/8$, (c) $\delta=6/8$, (d) $\delta=1$, (e) $\delta=11/8$, and (f) $\delta=12/8$ (AA').

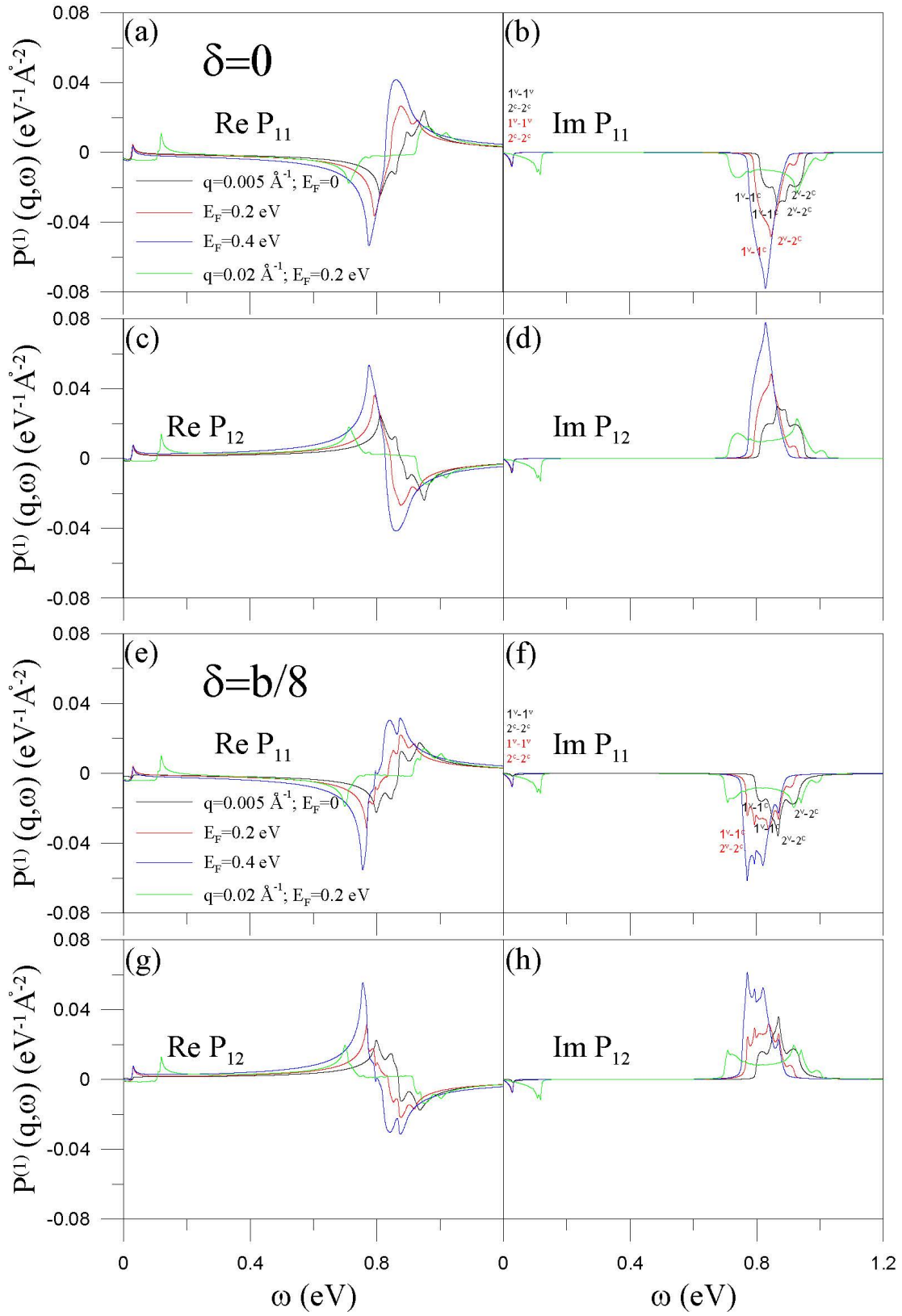


Figure 4: The two independent bare polarization functions under $[q=0.005 \text{ 1/\AA}, \phi = 0^\circ; E_F = 0, 2 \& 0.4 \text{ eVs}]$ and $[q=0.02 \text{ 1/\AA}; E_F = 0, 2 \text{ eV}]$ for the $\delta = 0$ bilayer stacking: (a) $Re[P_{11}]$, (b) $Im[P_{11}]$, (c) $Re[P_{12}]$, and (d) $Im[P_{11}]$. Similar plots of the $\delta = 1/8$ system in (e)-(h).

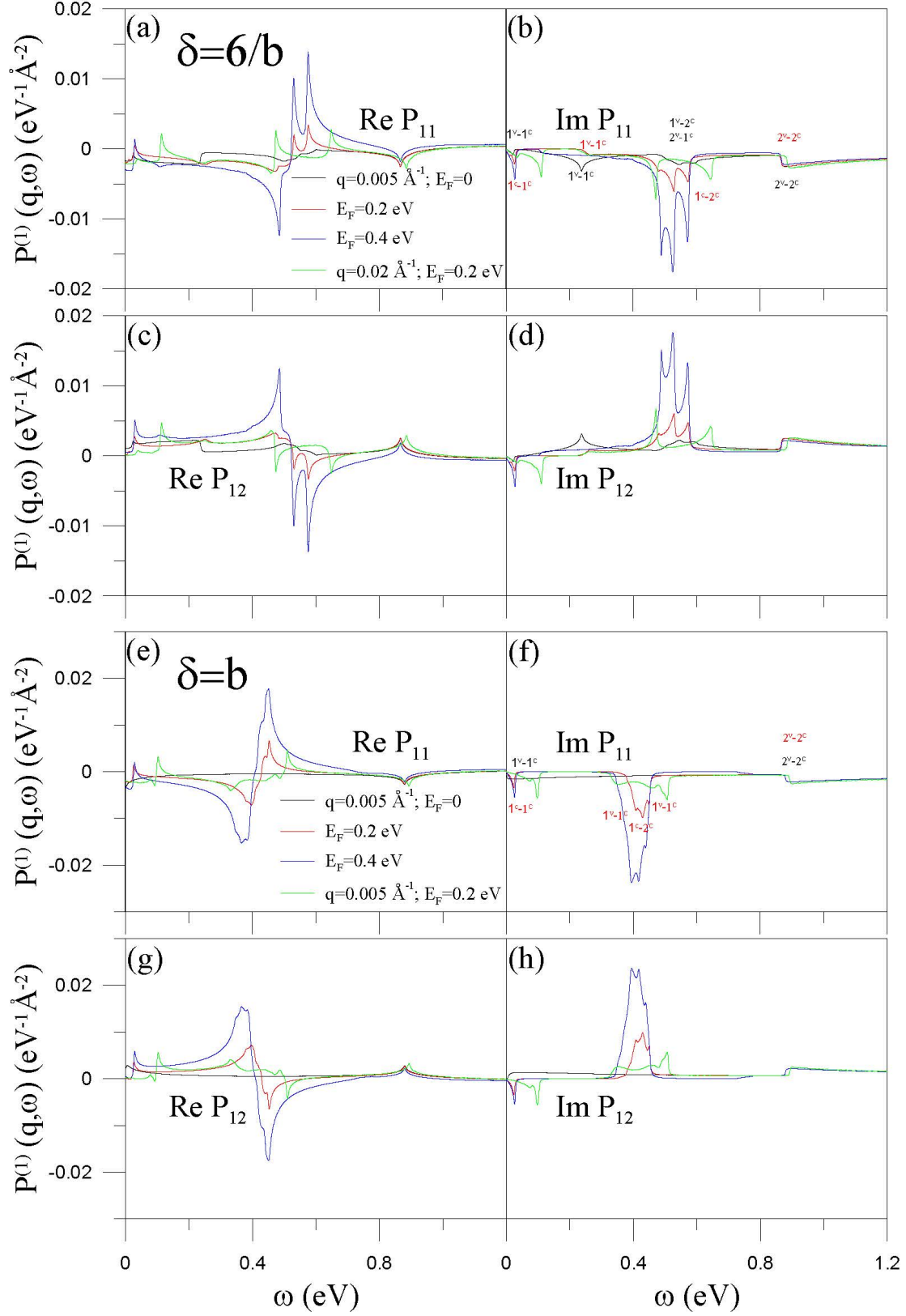


Figure 5: Similar bare response functions in Fig. 4, but displayed for the $\delta = 6/8$ and $\delta = 1$ bilayer graphenes in (a)-(d) and (e)-(h), respectively.

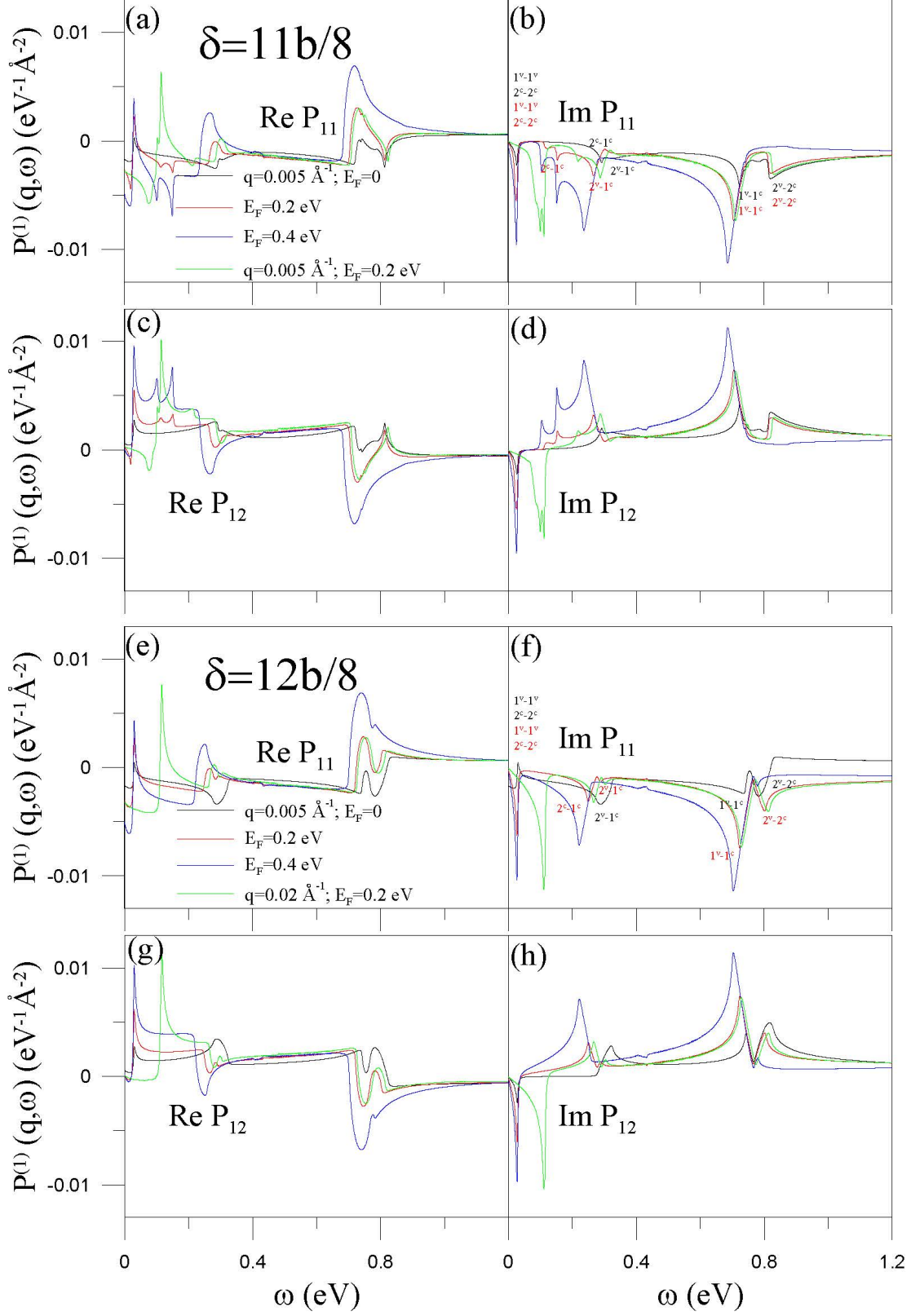


Figure 6: Similar single-particle excitation functions in Fig. 4, but illustrated by the $\delta = 11/8$ and $\delta = 12$ bilayer graphene systems, respectively, in (a)-(d) and (e)-(h).

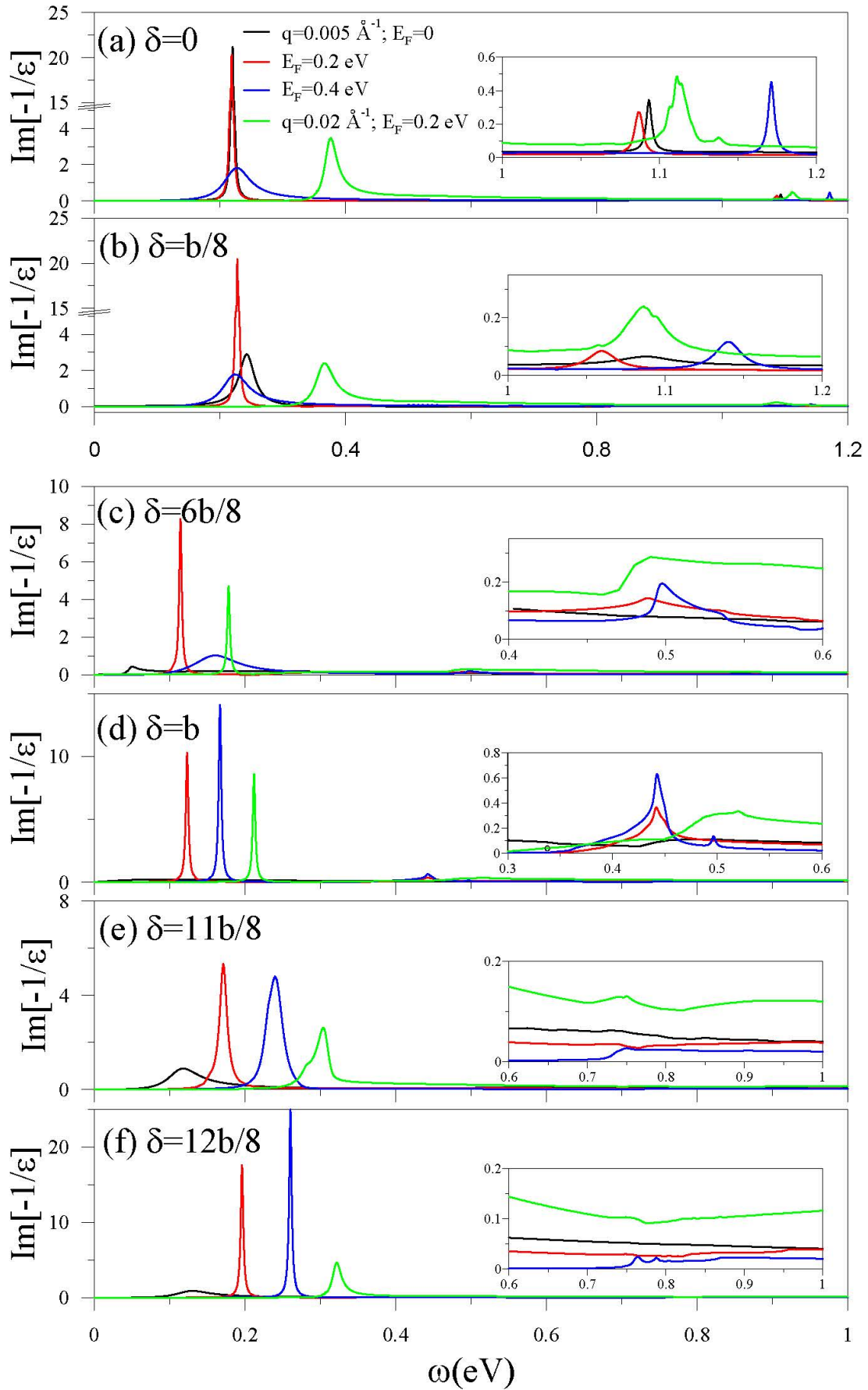


Figure 7: The energy loss spectra under [$q=0.0051/\text{\AA}$, $\phi = 0^\circ$, $E_F = 0, 0.2$ & 0.4 eVs] and [$q=0.02$ $1/\text{\AA}$; $E_F = 0, 2$ eV] for the sliding bilayer systems: (a) $\delta = 0$, (b) $\delta = 1/8$, (c) $\delta = 6/8$, (d) $\delta = 1$, (e) $\delta = 11/8$, and (f) $\delta = 12/8$. Also shown in the insets are the enlarged higher-frequency results.

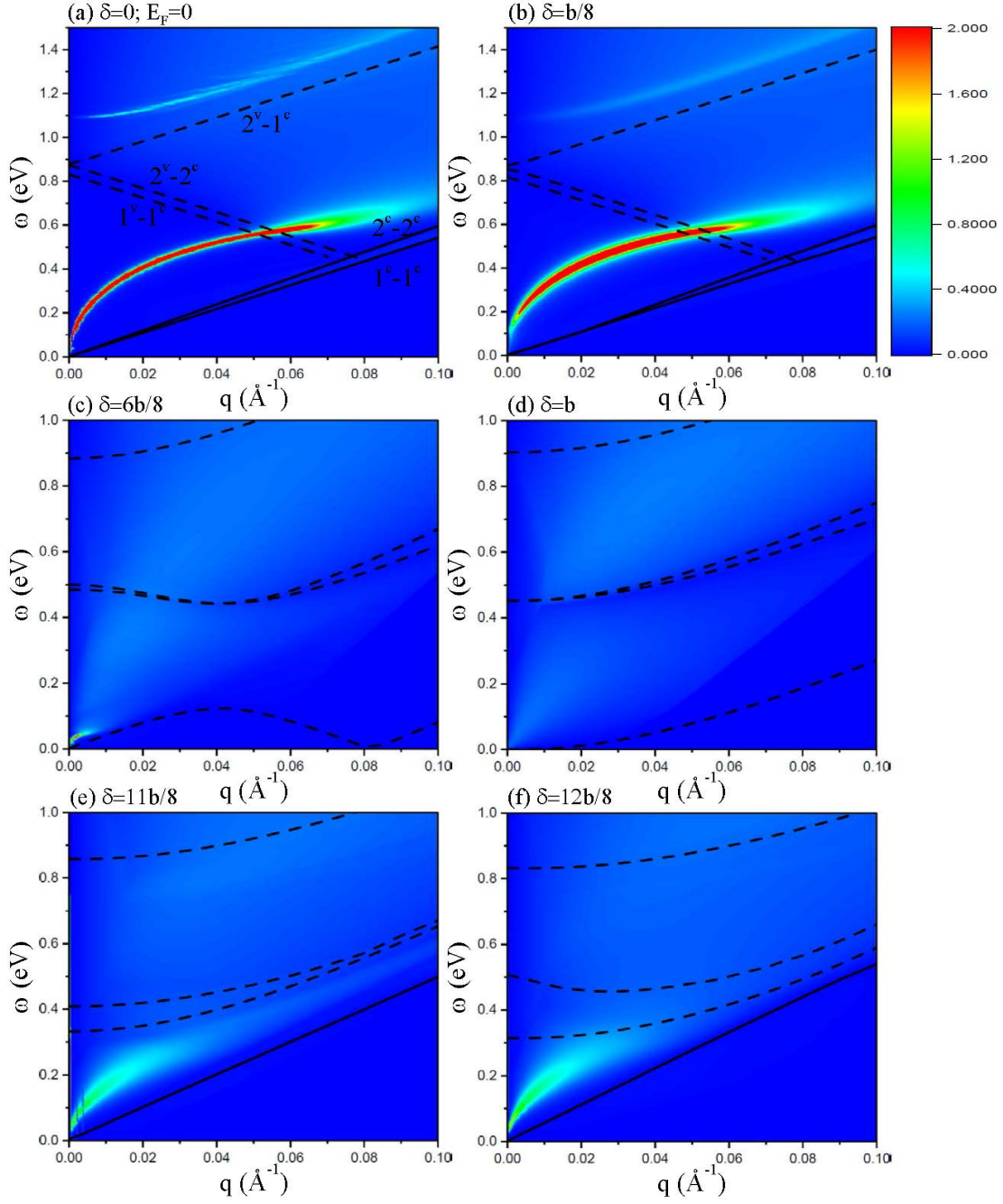


Figure 8: The (momentum, frequency)-phase diagrams of the pristine sliding bilayer graphenes: (a) $\delta = 0$, (b) $\delta = 1/8$, (c) $\delta = 6/8$, (d) $\delta = 1$, (e) $\delta = 11/8$, and (f) $\delta = 12/8$.

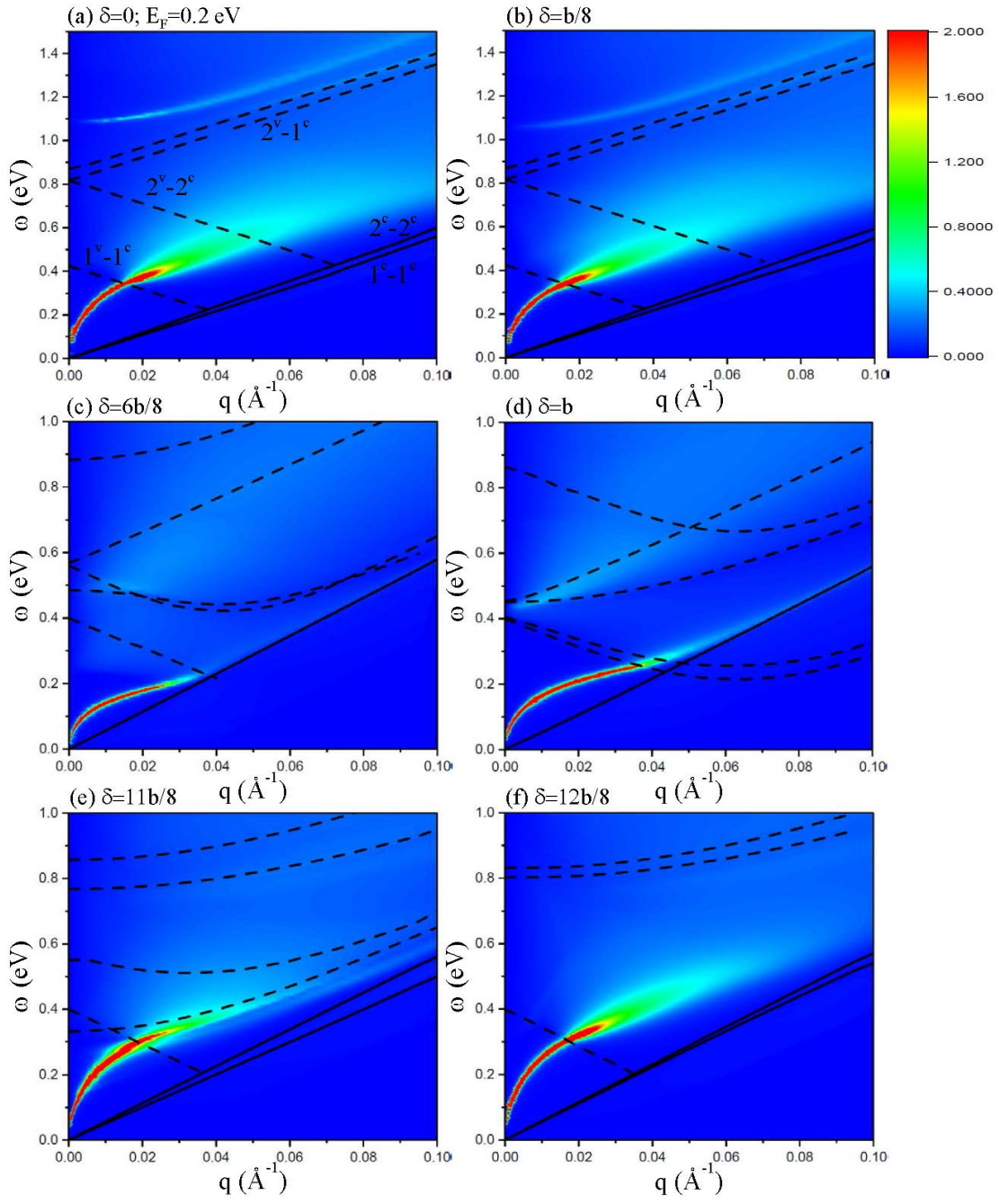


Figure 9: Similar plots as Figs. 8(a)-8(f), but shown for $E_F = 0.2$.

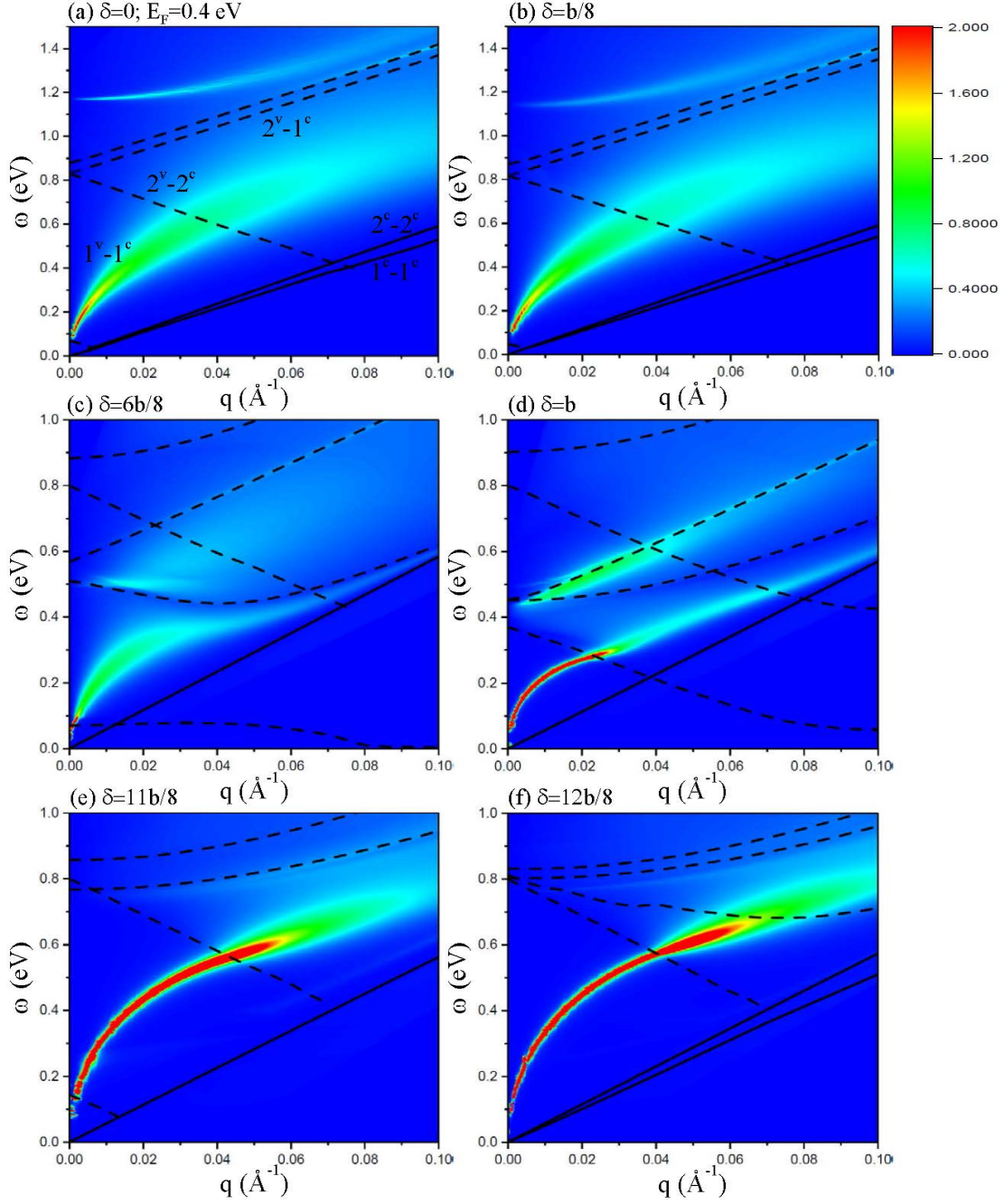


Figure 10: Similar plots as Figs. 9(a)-9(f), indicating the distinct doping effects at $E_F = 0.4$.